Influence of La and Si promoters on the anaerobic heterogeneous catalytic decomposition of ammonium dinitramide (ADN) via alumina supported iridium active sites

Merve Kurt [a], Zeynep Kap [a], Sinem Senol [a,c], Kerem Emre Ercan [a,b], Abel Tetteh Sika-Nartey [a], Yusuf Kocak [a], Ahmet Koc [b], Hacı Esiyok [b], Burcu Selen Caglayan [c,d], Ahmet Erhan Aksoylu [c,e], Emrah Ozensoy [a,f,*,1]

[a] Department of Chemistry, Bilkent University, 06800 Bilkent, Ankara, Turkey
[b] Roketsan Inc., 06780 Elmadag, Ankara, Turkey
[c] SNG&HydTec Lab, Kandilli Science and Technology Building, Bogazici University, 34684 Kandilli, Istanbul, Turkey
[d] Advanced Technologies R&D Center, Bogazici University, 34342 Bebek, Istanbul, Turkey
[e] Department of Chemical Engineering, Bogazici University, 34342 Bebek, Istanbul, Turkey
[f] UNAM-National Nanotechnology Center, Bilkent University, 06800 Bilkent, Ankara, Turkey

ABSTRACT

Structural origins of the promotional effects of the La or Si doping of alumina supported Ir catalysts in anaerobic ammonium dinitramide decomposition were investigated. Our findings reveal that Ir/Al_2O_3 and $Ir/La-Al_2O_3$ favorably lower the onset temperature of the ADN decomposition reaction, whereas Si doping boosts the pressure generation during the reaction. Formation of mostly metallic Ir nanoparticles for Ir/Al_2O_3 and $Ir/La-Al_2O_3$ enables the lowering of the activation energy of the reaction. On the other hand, enhancement due to Si promotion is associated to the generation of small oxidic Ir_n^{x+} clusters which are strongly interacting with the SiO_x-AlO_x surface domains of the support material. Fundamental structure-functionality relationships unraveled in the current work may allow design of novel catalytic systems for aerospace monopropellant propulsion systems with higher performance by simultaneous exploitation of Ir active sites with different electronic properties.

1. Introduction

Monopropellants constitute a promising family of fuels consisting of a single fuel formulation without a need for the use of a secondary oxidant. Historically, hydrazine (N_2H_4) has been the most commonly used monopropellant in aerospace applications for the trajectory control of the satellites in the low earth orbit [1,2]. However, hydrazine possesses significant health risks due to its high toxicity and carcinogenic nature [3]. In addition, storage, transport, refilling, and testing of hydrazine require not only complex but also costly processes and infrastructure. Accordingly, European Union (EU) Registration, Evaluation, Authorization and Restriction of Chemicals (REACH) regulation included hydrazine to the list of chemicals to be prohibited in the future by the European Chemicals Agency (ECHA) [4]. Along these lines, both National Aeronautics and Space Administration (NASA) and European Space Agency (ESA) declared interest in safe, high-performance, long-lasting, and environmentally friendly fuel alternatives called "Green Propellants" that can replace hydrazine in the future [5].

Ionic liquids (ILs) are versatile materials that find use in a multitude of technological applications [6] such as catalysis, separation technologies, sensors, solid state devices, and aerospace due to their unique properties such as low vapor pressure, liquidity within a wide temperature range, high thermal stability, ionic conductivity, fine-tunable chemical structure, adjustable viscosity, density, and gas permeability [6]. Energetic Ionic Liquids (EILs) typically have high nitrogen and oxygen content, and beneficial chemical/physical properties rendering them potentially useful in propulsion systems [7]. Furthermore, storage, transport, and processing of EILs are much safer, economical, and easier than hydrazine. Hence, aerospace fuel formulations used in the next generation satellite propulsion systems are expected to exploit EILs such

---

as ammonium dinitramide (ADN, $[NH_4^+][N(NO_2)_2^-]$), hydroxylammonium nitrate (HAN, $[NH_3OH^+][NO_3^-]$) [8,9], hydrazinium nitroformate (HNF, $[H_2NNH_3^+][C(NO_2)_3^-]$) [10], or ammonium nitrate (AN, $[NH_4^+][NO_3^-]$) [11], where particularly, ADN attracts significant attention in the recent years [12–15]. EILs can be decomposed either non-catalytically at high temperatures or via heterogeneous catalysts in a controlled and efficient manner at lower temperatures. The design and development of highly active, thermally stable, and durable heterogeneous catalysts are challenging due to the large amount of heat generated during the exothermic ADN decomposition. Alumina is the most commonly used catalyst support material for the catalytic hydrazine and ADN decomposition. However, at elevated temperatures, conventional alumina polymorphs sinter and lose their specific surface area (SSA) which also result in the decrease in porosity and catalytic activity [16]. Conventional ADN and HAN decomposition catalysts are typically comprised of platinum group metal (PGM) catalytic active sites (e.g., Ir, Pt etc.) dispersed on alumina or hexaaluminates [8,9,12,17]. Among the platinum group metals, iridium is widely used in high temperature applications due to its high melting point and high Tammann temperature [18–23]. Thus, in order to boost the catalytic performance of Ir active sites and enhance the thermal stability of the catalytic architecture, alumina support materials can be promoted with various elements such as La and Si [24–29]. It is well known that La promotion of alumina may enhance the surface dispersion of PGM active sites via strong metal support interaction (SMSI) and modify the electronic structure of the PGM active sites [27,29], while Si promotion may increase the surface acidity of the alumina support which may result in alteration of the PGM electronic structure as well as the nature and strength of the interaction between the reactants and intermediates with the support material [26, 28].

Along these lines, in the current work, we focus on the influence of two different catalytic promoters (i.e., La or Si incorporated into the alumina support material) on the catalytic performance of Ir active sites in anaerobic ADN decomposition. Through detailed in-situ/ex-situ spectroscopic, diffraction and microscopic investigations, we demonstrate that La or Si incorporation into the alumina support material leads to different types of catalytic performance enhancement of the Ir active sites. While La promotion preserves the catalytic onset temperature of Ir/Al$_2$O$_3$, Si promotion results in a boost in the total pressure generation upon ADN decomposition. Current results provide valuable scientific insights regarding the molecular level origins of these different promotional effects by shedding light on new catalytic structure-functionality relationships.

2. Experimental section

2.1. Materials and synthesis

Catalysts used in the current work were in the form of 5Ir/Al$_2$O$_3$ and 5Ir/X-Al$_2$O$_3$ with a nominal Ir content of 5 wt% (experimentally determined Ir contents are given in the forthcoming sections), where X corresponded to either La or Si. Accordingly, alumina and two different types of doped alumina support materials (La-Al$_2$O$_3$ and Si-Al$_2$O$_3$) were utilized to synthesize the catalysts. These particular doping agents were chosen not only to modify the electronic properties of the catalytically active Ir sites but also to alter the surface chemistry of the support material and strengthen its thermal stability. The latter argument was also verified by the specific surface area (SSA) data of the doped alumina support materials in their fresh forms (350 m^2/g for Si-Al$_2$O$_3$ and 140 m^2/g for La-Al$_2$O$_3$) as well as after 24 h thermal aging in air at 1200 °C (80 m^2/g for Si-Al$_2$O$_3$ and 40 m^2/g for La-Al$_2$O$_3$). On the other hand, the surface area of the bare alumina was 150 m^2/g which decreased to 20 m^2/g after thermal aging at 1200 °C (Fig. S1). It is clear that promotion of alumina with La or Si is critical to preserve SSA values of the support material and prevent thermal aging after high-temperature operation. In the current work, we focus on the fresh catalysts and leave the behavior

of the thermally aged catalysts to a forthcoming report.

5Ir/Al$_2$O$_3$ and 5Ir/X-Al$_2$O$_3$ catalysts were synthesized using incipient to wetness impregnation method. Ir sites were incorporated on the support materials in two successive impregnation cycles. In the typical synthesis of a 1.050 g of catalyst sample, firstly 0.0407 g of IrCl$_3$ precursor (IrCl$_3$•xH$_2$O, Sigma Aldrich, reagent grade) corresponding to 2.5 wt% Ir loading was dissolved in NH$_3$(aq) (Sigma Aldrich, ACS reagent, 28.0–30.0% NH$_3$ basis) solution with a pH of 9.4 and impregnated onto each of the support materials. The synthesized materials were dried at 60 °C in air for 8 h. After these initial impregnation and drying steps, two different preparation protocols were carried out. In the first protocol: i) catalysts were calcined in air at 400 °C for 3 h, ii) impregnated with a second loading of 2.5 wt% Ir, dried at 60 °C in air for 8 h, and calcined in air at 400 °C for 3 h, and iii) finally reduced at 500 °C for 2 h under 100 ml/min 5% H$_2$/Ar (Linde GmbH) flow. Catalysts synthesized using this first protocol are designated in the text as "*CCR*" (e.g., 5Ir/La-Al$_2$O$_3$ *CCR*). In the second protocol: i) impregnated catalysts were reduced at 500 °C for 2 h under 100 ml/min 5% H$_2$/Ar flow, ii) impregnated with a second loading of 2.5 wt% Ir, dried at 60 °C in air for 8 h, and reduced at 500 °C for 2 h under 100 ml/min 5% H$_2$/Ar flow. Catalysts synthesized using this second protocol are designated in the text as "*RR*" (e.g., 5Ir/Si-Al$_2$O$_3$ *RR*). ADN monopropellant fuel mixture contained 63.0 wt% ADN, 18.4 wt% methanol, 14.0 wt% water, 4.6 wt% ammonia. The oxygen balance for the pure and the ADN solution were + 25.8% and − 17.8%, respectively.

2.2. In-situ and ex-situ characterization experiments

X-ray diffraction (XRD) measurements were performed using a Panalytical X'PertPro Multipurpose X-Ray Diffractometer with a CuKα1 X-Ray source (40 kV, 45 mA, λ = 1.5405 Å). Williamson-Hall analysis was carried out by using Rigaku Smartlab program.

SSA of the samples were measured via the five-point Brunauer-Emmett-Teller (BET) method by low temperature isothermal adsorption/desorption of N$_2$(g) (purity > 99.99%, Linde GmbH). Prior to BET measurements, samples were degassed in vacuum at 300 °C for 2 h. BET analyses were carried out using a Micromeritics ASAP 2000 gas sorption and porosimetry system.

Bright field transmission electron microscopy (TEM) images were acquired using a Hitachi HT7700 Transmission Electron Microscope with an electron beam energy of 120 kV. Particle size calculations were done from 100 particles with ImageJ software.

Energy dispersive X-ray (EDX) analyses were performed via a FEI-Quanta 200 FEG ESEM with an electron energy of 20 keV.

Quantification of iridium loadings in the bulk of the catalysts were carried out via a Bruker S2 PUMA Energy Dispersive X-ray Fluorescence (EDXRF) spectrometer which was equipped with a silicon drift detector and a silver X-ray source (maximum power, 50 kV). For the XRF analysis, samples were packed in a loose powder form and measurements were performed under He atmosphere.

X-ray photoelectron spectroscopy (XPS) experiments were performed with a SPECS PHOIBOS hemispheric energy analyzer. Monochromatic Al-Kα X-ray source (14 kV, 400 W) was used during the XPS data collection. Data analysis was performed using CasaXPS (v2.3.23rev 1.1G) software. Binding energy (B.E.) calibration was performed using the C1s signal at 284.8 eV.

Pyridine adsorption experiments via in-situ Fourier transform infrared (FTIR) spectroscopy were done by using a custom design in-situ FTIR cell equipped with a pyridine vapor doser and a rotary vane pump for evacuation. Samples were pressed on a tungsten grid and placed into the in-situ FTIR cell. Before pyridine adsorption experiments, each sample was annealed under vacuum at 500 °C for 5 min with a heating ramp of 12 °C /min to activate the surfaces. 20 Torr pyridine vapor was dosed over the samples for 30 min and the in-situ FTIR spectra were recorded after evacuation of pyridine for 15 min.

Relative ADN adsorption/uptake amounts of the catalyst samples

were determined in a semi-quantitative fashion using a Bruker Alpha-II Platinum Attenuated Total Reflectance (ATR)-IR spectrometer. Prior to these measurements, 3 mg of a catalyst sample was mounted on a tungsten grid. Then, the samples were dipped into a saturated ADN-water mixture (7 g ADN dissolved in 10 ml water) for 1 min. Next, the catalyst sample was dried under air, followed by acquisition of the ATR-IR spectra.

CO adsorption experiments via in-situ Fourier transform infrared (FTIR) spectroscopy were executed in transmission mode in a custom-design batch-type in-situ spectroscopic reactor coupled to a Bruker Tensor 27 FTIR spectrometer equipped with a liquid nitrogen-cooled mercury cadmium telluride (MCT) IR detector. The in-situ spectroscopic reactor was also connected to a quadruple mass spectrometer (QMS, Stanford Research Systems, RGA 200) for temperature programmed desorption (TPD) measurements. Instrumental details of the currently performed in-situ FTIR and TPD experiments can be found elsewhere [30]. Before the CO adsorption experiments, each sample was activated via an initial treatment including annealing at 500 °C for 10 min in 5 wt% H_2/Ar mixture (Linde GmbH) with a total pressure of 10 Torr. Then the sample was cooled to 50 °C and the reactor was evacuated to 10^{-3} Torr. Next, catalyst sample was exposed to various pressures ($P_{CO(g)} = 0.01, 0.04, 0.2, 0.9, 12.0, 36.5$ Torr) of CO (g) (Linde GmbH, purity > 99.99%) and kept at each pressure for 10 min at 50 °C. As the last adsorption step, sample was exposed to 60 Torr CO for 30 min to saturate the surface with CO. After each CO exposure, the spectroscopic reactor was evacuated and in-situ FTIR spectra were recorded with a frequency resolution of 1 cm^{-1} and by averaging 128 scans per spectrum. CO TPD experiments were performed with 5 Torr CO at 50 °C for 30 min followed by evacuation of the reactor to 10^{-3} Torr. During the TPD runs, catalyst samples were heated from 50 °C to 500 °C with a linear heating rate of 12 °C /min^{-1} in vacuum.

Surface dispersion of Ir and the total number of Ir actives sites on the catalyst surfaces were determined via CO chemisorption method by using a Hiden Analytical CATLAB mass spectroscopic instrument. Prior to measurements, samples were reduced in-situ at 500 °C under 5% H_2/He flow and then cooled to 35 °C. CO uptake measurements were performed at 35 °C under 60 ml/min He flow and injection of 0.1 ml pulses of 5% CO over the catalyst samples. In the dispersion calculations, a CO/Ir stoichiometry of 1 was assumed [31,32].

In an attempt to elucidate the electronic structural changes occurring on the Ir active sites during the *CCR* and *RR* catalyst preparation protocols, in-situ extended X-ray absorption fine structure (EXAFS) and in-situ x-ray absorption near edge spectroscopy (XANES) experiments were designed and carried out at the ROCK beamline of the Soleil Synchrotron Facility (Saint-Aubin, France). EXAFS and XANES data were collected for the Ir L_{III} edge of the synthesized catalysts. Quick EXAFS (QEXAFS) monochromator was utilized to monitor the time-resolved changes in the Ir L_{III} edge as a function of treatment conditions [33]. The Ir L_{III} edge energy (11215 eV) was calibrated using a metallic Ir reference foil. Each XANES/EXAFS spectrum for a given catalyst sample was acquired by averaging 1200 scans. In the EXAFS analysis, the forward Fourier transform range was determined to be within 3–17 $Å^{-1}$, where 1–3 $Å^{-1}$ range was used as the fitting (backward Fourier transform) interval. Ir was chosen as the main absorber in the fitting of the EXAFS data. EXAFS/XANES data analysis were carried out by using the IFEFFIT tool of the Demeter software package [34]. For the in-situ EXAFS/XANES measurements, catalyst samples were mounted in a spectroscopic flow reactor equipped with a custom-design capillary flow cell which was heated via a gas blower heating system [35]. This setup allowed exposure of the catalyst surfaces to reducing or oxidizing conditions with a gas mixture of desired composition, flow rate and temperature during the XANES/EXAFS measurements.

In-situ XANES/EXAFS experiments were carried out using two different experimental procedures. The first procedure was designed to mimic the synthesis protocol of the catalysts classified with the "*CCR*" code. Here, the support materials were impregnated with 2.5 wt% Ir,

dried in air at 60 °C for 8 h and calcined in air at 400 °C for 3 h. This is followed by the second loading of 2.5 wt% Ir and drying in air at 60 °C for 8 h. These samples were placed into the in-situ capillary XANES/EXAFS flow cell. Next, the sample was exposed to 20% O_2/Ar gas mixture with a flow rate of 30 ml/min and heated from RT to 400 °C using a heating rate of 7 °C/min in this gas mixture. After waiting 10 min at 400 °C, sample was cooled to RT and the gas mixture was switched to 5% H_2/Ar (flow rate = 30 ml/min) and the catalyst was heated to 500 °C with a heating rate of 7 °C/min. Then the sample was cooled to RT in 5% H_2/Ar after waiting 10 min at 500 °C, and in-situ XANES/EXAFS data were collected for the *CCR* samples at RT. To imitate the "re-oxidation" of the *CCR* samples under ambient conditions after the completion of the catalyst synthesis protocol, gas composition was switched to 20% O_2/Ar (flow rate = 30 ml/min) at RT and a second set of in-situ XANES/EXAFS data were collected at RT.

The second in-situ XANES/EXAFS experimental procedure was designed to mimic the synthesis protocol of the catalysts denoted with the "*RR*" code. In this procedure, the support materials were impregnated with 2.5 wt% Ir, dried in air at 60 °C for 8 h and reduced under 100 ml/min 5% H_2/Ar flow at 500 °C for 2 h. This is followed by the second loading of 2.5 wt% Ir and drying in air at 60 °C for 8 h. These samples were placed into the in-situ capillary XANES/EXAFS flow cell. Then, the catalysts were heated from RT to 500 °C with a heating rate of 7 °C/min in 5% H_2/Ar (flow rate = 30 ml/min). Then the catalysts were kept at 500 °C for 10 min, followed by cooling to RT in this gas mixture, where the in-situ XANES/EXAFS data for the *RR* catalysts were collected. Re-oxidation of the *RR* samples were also investigated by switching the gas composition to 20% O_2/Ar (flow rate = 30 ml/min) at RT and subsequent in-situ XANES/EXAFS data acquisition at RT.

2.3. Catalytic performance tests

Performance of the synthesized catalysts in the anaerobic decomposition of ADN were investigated using custom-design batch-type catalytic reactors (Fig. 1a–c). Reactors were optimized to work within a pressure range of 0.01–5.00 bar and a temperature range of RT-400 °C. Three identical individually controlled reactors were built to enable parallel operation. Two different K-type thermocouple (TC) temperature sensors were positioned at different locations in each reactor (i.e., at the catalyst bed and in the gas chamber). For pressure measurements, two different types of pressure gauges were utilized. One of these gauges (Keller, PAA-23SY) allowed high-speed (2 kHz) measurement of the reactor pressure within 0.01–2.00 bar and the other one (Edwards, APG100-XLC) enabled measurement of low pressures (10^{-4}-1.00 mbar) upon evacuation. An automated Kloehn syringe pump (V6 48K Syringe Drive Pump) with 48,000 steps was used to inject the fuel into the reaction compartment in each reactor with high accuracy and reproducibility. Temperature of the reaction compartment was regulated via PID controllers. Temperature and pressure data collection was carried out via a custom-design software which was capable of high-speed data logging.

In a typical catalytic ADN decomposition test, a 100 mg catalyst sample was placed in the reaction compartment of the batch reactor. Then, the reactor was filled with Ar(g) ($P_{Ar(g)} = 1$ bar) to obtain an inert/anaerobic atmosphere and 130.00 ± 0.02 μl of ADN was injected onto the catalyst powder at RT. Next, computer-controlled temperature ramp was initiated. Time-dependent pressure and temperature data were recorded during the heating ramp. Fig. 2 shows typical temperature vs. time and pressure vs. time plots obtained from one of the batch reactors during a catalytic ADN decomposition run. The onset temperature (T_{Onset}), ΔP_{max}, and ΔP_{eq} values were used to compare relative performances of the catalysts in the catalytic anaerobic decomposition of ADN. T_{Onset} value obtained from the temperature vs. time plot (revealing the triggering of the ADN decomposition reaction). ΔP_{max} and ΔP_{eq} values acquired from the pressure vs. time plot show the generated maximum pressure and the equilibrium pressure, respectively. A lower
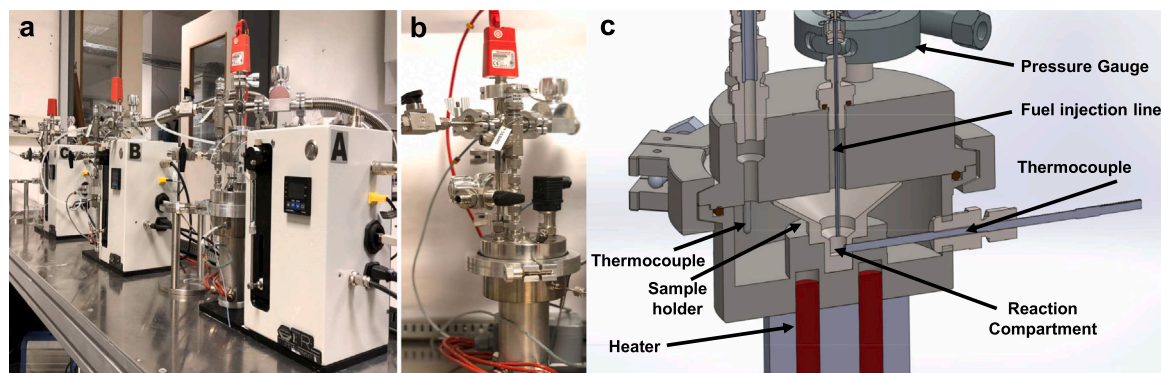
Fig. 1. (a and b) Overall view, and (c) the detailed interior design of the custom-made parallel batch reactors used in the catalytic anaerobic decomposition of ADN.
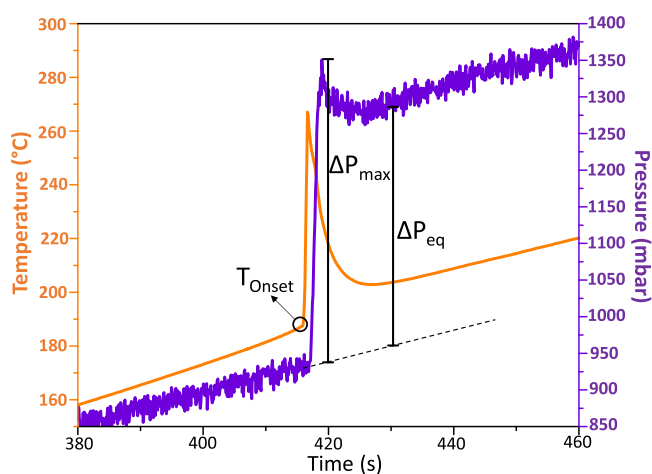

Fig. 2. Typical temperature vs. time and pressure vs. time plots obtained during a catalytic anaerobic ADN decomposition run.

T_{Onset} value signifies diminishing of the apparent activation energy of the reaction and a greater ΔP values contributes to an enhanced thrust. Moreover, the number of moles of gas (n_{gas}) generated as a result of ADN decomposition was also calculated from the perfect gas equation by using the temperature of the gas phase, equilibrium pressure and the volume of the reactor (175 ml). Note that in a typical experiment, the injection of 130 μl of the fuel mixture (with a density of $\rho = 1.24$ g/ml at 298 K) contained 101.6 mg (or 0.82 mmol) of ADN.

Simultaneous Differential Scanning Calorimetry/Thermogravimetric Analysis (DSC/TGA) experiments were performed by using a TA instruments SDT 650 device. During these measurements, 3 mg catalyst was placed into the hermetic aluminum pan which can resist up to 3 bar of internal pressure and 1 μl ADN-based fuel was introduced on to the catalyst with a micropipette. Samples were analyzed from RT to 250 °C with a heating rate of 4 °C/min in N_2 flow (30 ml/min). Onset temperature (T_{Onset} (°C)) and Energy (ΔH (J/g)) generated as a result of ADN decomposition per mass of fuel mixture used were determined from the DSC curve as shown in Fig. S2. Moreover, gas phase decomposition products were investigated by connecting the heated DSC/TGA exhaust gas line to an online Bruker FTIR spectrometer equipped with an IR gas cell.
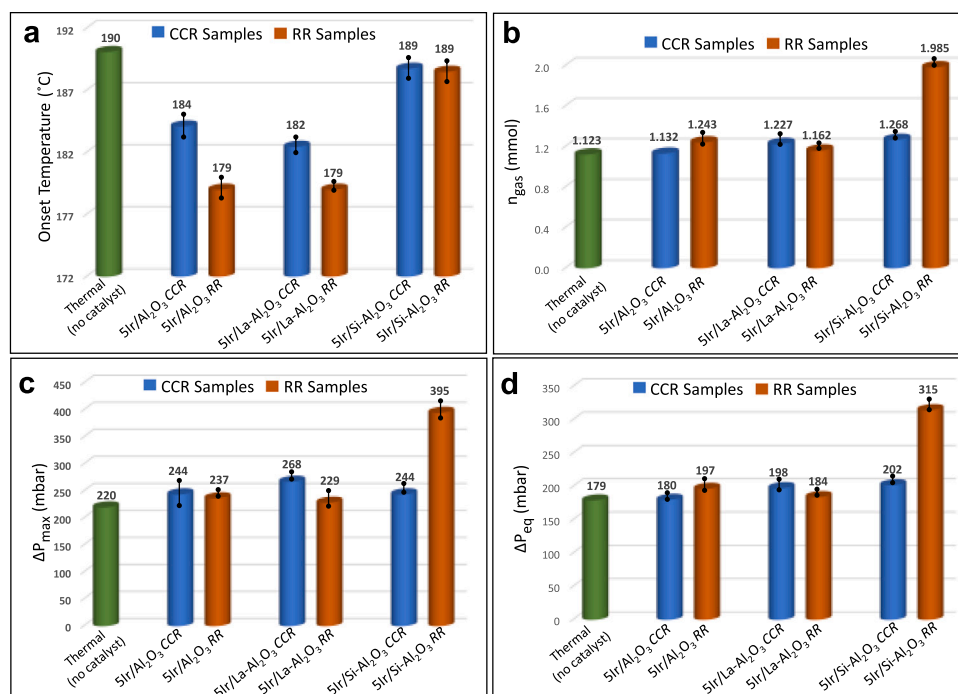

Fig. 3. (a) Onset temperature (T_{Onset}), (b) number of moles of gas (n_{gas}) generated, (c) maximum pressure generation (ΔP_{max}), and (d) equilibrium pressure (ΔP_{eq}) difference values obtained in the anaerobic catalytic decomposition tests for ADN with the synthesized catalysts and without a catalyst.

3. Results and discussion

3.1. Catalytic anaerobic ADN decomposition tests

Fig. 3a–d show the T_{Onset}, ΔP_{max}, ΔP_{eq}, and n_{gas} values obtained during the anaerobic decomposition of ADN in the presence of the synthesized catalysts as well as in the absence of a catalyst. In the absence of a catalyst, thermal decomposition of ADN starts at 190 °C, yielding a decomposition related pressure generation of 220 mbar. Corresponding temperature vs. time and pressure vs. time plots for these results are also presented in Figs. S3-S6 of the supporting information (SI) section. As can be seen in Fig. 3a, synthesis protocol (*CCR* vs. *RR*) has a relatively minor effect on T_{Onset}. Undoped and La promoted alumina are more effective in decreasing the T_{Onset} values, whereas Si promotion is more efficient in increasing ΔP_{max} and ΔP_{eq} values as shown in Fig. 3c and d, respectively. It is worth emphasizing that the catalytic performance trends obtained in the batch reactor results are in good agreement with the corresponding T_{Onset} and ΔH trends obtained via DSC measurements as shown in Fig. S7-S11. In addition, Table S1 compares the maximum decrease in the onset temperature of the ADN decomposition in the presence of a catalyst as opposed to ADN decomposition in the absence of a catalyst presented in the current work with that of the former studies in the literature.

Gas phase FTIR spectra for the IR-active gases produced as a result of the catalytic and non-catalytic decomposition of ADN-based propellant at the corresponding T_{Onset} values given in Fig. S7a are shown in Fig. S12. The detected gaseous species were N_2O, NH_3, CO_2, CH_3OH, H_2O, NO, NO_2 [36–38]. Complete decomposition reaction of ADN into thermodynamic products is presented in Eq. (1);

$$NH_4N(NO_2)_2(aq) \rightarrow 2\ N_2(g) + 2\ H_2O(g) + O_2(g) \qquad (1)$$
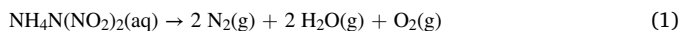
Hence, a complete decomposition of 0.82 mmol ADN is expected to generate 4.1 mmol of gaseous products. In the current work, the largest n_{gas} value of 1.99 mmol was obtained for the 5Ir/Si-Al$_2$O$_3$ *RR* catalyst (Fig. 3b) suggesting that complete decomposition of the ADN mixture was not achieved.

These observations point out to a variety of factors which may be associated with the origins of these dissimilar promotional behaviors such as: i) variations in the crystallographic phases of alumina upon doping with La or Si, ii) distribution and particle size of Ir active sites on the support surfaces, iii) oxidation state of the Ir species, iv) interaction strength between the Ir active sites and the support material, and v) nature of the coordination of the Ir atoms. Thus, in an attempt to shed light on these important structural and electronic factors which may be associated with the observed catalytic promotional effects, we performed detailed ex-situ and in-situ characterization experiments.

3.2. Crystal structure via XRD

Variations in the crystallographic properties of the synthesized catalysts as a function of promoter type and the synthesis protocol were examined in XRD studies (Figs. 4a-b). XRD patterns of the support materials are also given in Fig. S13. As can be seen in Fig. 4a, *CCR* synthesis protocol leads to sharp and strong metallic Ir diffraction signals for all samples, suggesting the presence of relatively large Ir nanoparticles. Unfortunately, due to the overlap between alumina and Ir diffraction signals, reliable average Ir particle size determination via XRD data analysis was not feasible. Also, note that no oxidic Ir species are visible in the XRD data given in Fig. 4a. It is important to mention that considering the large Ir loading of the synthesized catalyst samples, presence of additional disordered metallic and/or oxidic Ir species with smaller particle sizes which are not detectable via XRD cannot be ruled out. This argument will be further verified via current TEM and in-situ FTIR results presented in the forthcoming sections. Another important aspect of Fig. 4a is the difference in the alumina support crystal structure as a function of promoter type. It is apparent that while Si promotion results in exclusively γ-Al$_2$O$_3$ phase, bare and La promoted alumina yield both δ-Al$_2$O$_3$ and γ-Al$_2$O$_3$ phases. This observation is consistent with the aforementioned SSA values of the corresponding support materials. It is known that alumina materials derived from boehmite precursor consecutively acquires γ → δ → θ → α crystallographic phases with increasing temperatures, where the corresponding SSA values monotonically decrease during these successive polymorphic phase transitions [39]. Thus, as will be discussed in the next section, observation of a δ-Al$_2$O$_3$ phase for the 5Ir/Al$_2$O$_3$ and 5Ir/La-Al$_2$O$_3$ catalysts is consistent with the lower SSA value of this catalyst, as compared to that of the higher surface area 5Ir/Si-Al$_2$O$_3$ catalyst, where no alumina phases other than γ-Al$_2$O$_3$ phase were detectable in the latter case.

XRD patterns of the *RR* catalysts depicted in Fig. 4b indicate a striking difference in the crystallographic structure of the Ir species on these catalysts as opposed to that of *CCR* catalysts given in Fig. 4a. It is visible in Fig. 4b that *RR* synthesis protocol does not lead to noticeable diffraction signals neither for metallic nor for oxidic Ir species. Lack of metallic Ir species is also explicitly shown in the inset of Fig. 4b. These observations imply that Ir species predominantly exist as rather small (< 1 nm) clusters and to a lesser extent medium size (2–5 nm) nanoparticles on the *RR* catalysts.

3.3. Specific surface area

SSA measurement results for the synthesized catalyst samples are presented in Fig. 5. It is clearly discernible that the Si promotion has a stark influence on the SSA values while the La promotion does not affect
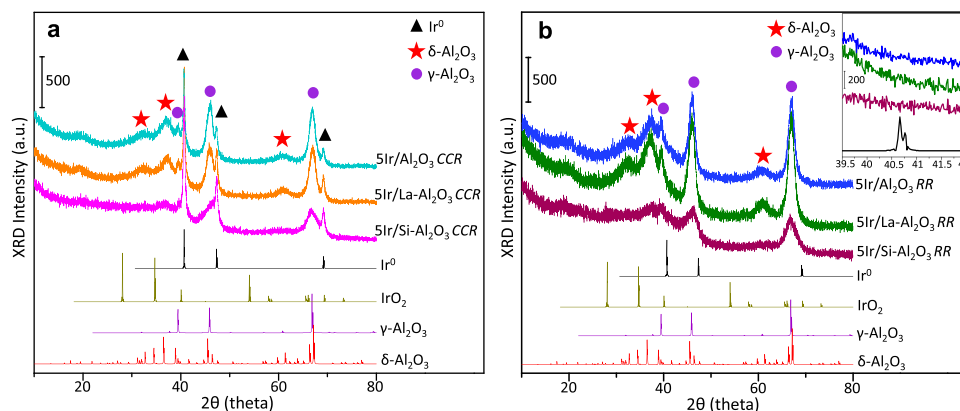

Fig. 4. XRD data for the synthesized catalysts and the corresponding reference phases. (a) 5Ir/Al$_2$O$_3$ *CCR*, 5Ir/La-Al$_2$O$_3$ *CCR*, and 5Ir/Si-Al$_2$O$_3$ *CCR*, (b) 5Ir/Al$_2$O$_3$ *RR*, 5Ir/La-Al$_2$O$_3$ *RR*, and 5Ir/Si-Al$_2$O$_3$ *RR*. (ICDD for Ir^0: 00-006-0598, ICDD for γ-Al$_2$O$_3$: 00–046–1212, ICDD for δ-Al$_2$O$_3$: 00–056–1186, ICDD for IrO$_2$: 00-015-0870).
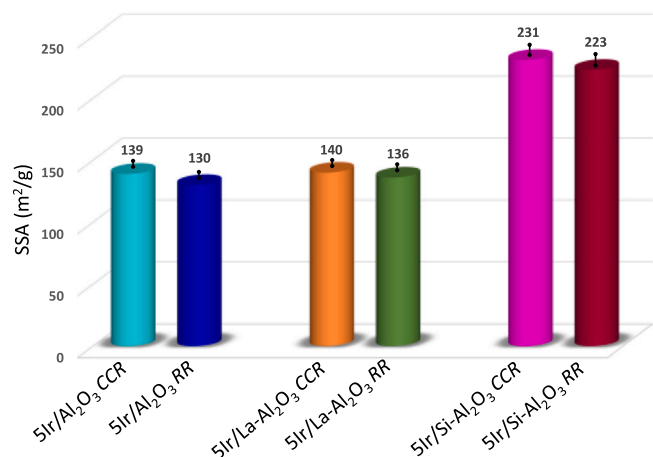
Fig. 5. BET surface areas for the synthesized catalysts.

the surface area. Also, variations in the synthesis protocol have a negligible effect. SSA values of the unpromoted 5Ir/Al$_2$O$_3$ *CCR* and *RR* catalysts are 139 and 130 m^2/g, respectively. For promoted samples, 5Ir/Si-Al$_2$O$_3$ *CCR* and *RR* catalysts possess SSA values of 231 and 223 m^2/g, whereas 5Ir/La-Al$_2$O$_3$ *CCR* and *RR* catalysts have SSA values of 140 and 136 m^2/g, respectively.

3.4. Ir Particle size analysis via TEM

Typical particle sizes of Ir species and their distribution on the promoted alumina support materials were investigated via TEM (Fig. 6a–f). TEM images of the *CCR* catalysts (Fig. 6a–c) indicate the presence of large Ir nanostructures having diameters ranging within 25–200 nm. This observation is also in accordance with the XRD data given in Fig. 4a revealing the presence of sharp and intense metallic Ir diffraction signals for *CCR* catalysts. Existence of Ir in these nanostructures were also verified by EDX and XRF measurements (Fig. 7 and Table S2). However,

it should be emphasized that the number density of such large Ir nanostructures on the *CCR* catalysts are rather low and additional Ir nanostructures are also visible with much smaller particle sizes (2–10 nm) indicating the existence of a multimodal distribution of Ir particles on all *CCR* catalysts. Furthermore, considering the high loading of Ir (5 wt% nominal and approximately 2.5 wt% experimental) in the catalyst formulation as well as the overall low surface density of the large Ir nanostructures in TEM, presence of small Ir clusters with particle sizes less than 1 nm which cannot be resolved with the currently used TEM should not be ruled out for the *CCR* catalysts.

Fig. 6d–f depict TEM images of *RR* catalysts. As expected from the lack of any discernible Ir diffraction signals in the corresponding XRD data of these catalysts (Fig. 4b), TEM images of the *RR* catalysts do not reveal any large Ir nanoparticles but instead are comprised of finely dispersed small (2–5 nm) Ir nanostructures. Again, possible existence of even smaller (< 1 nm) Ir clusters cannot be precluded on the *RR* catalysts due to the high Ir loading used in the catalyst synthesis and the moderate spatial resolution of the currently used TEM.

For the RR samples, ImageJ software was used to calculate the average Ir particle diameters from the TEM images (Fig. S14). The average diameters of the Ir particles were found to be 2.3 nm, 1.5 nm, and 1.6 nm for 5Ir/Al$_2$O$_3$ *RR*, 5Ir/La-Al$_2$O$_3$ *RR*, and 5Ir/Si-Al$_2$O$_3$ *RR* samples, respectively. On the other hand, because of the bimodal distribution of the Ir particles in CCR samples, we did not attempt to estimate the average Ir particle diameters for these samples via from TEM, rather, Williamson-Hall method was used to determine the average Ir crystallite size by using the XRD data given in Fig. 4a. The mean Ir crystallite diameters were estimated to be 50 nm, 18 nm, and 11 nm for 5Ir/Al$_2$O$_3$ *CCR,* 5Ir/La-Al$_2$O$_3$ *CCR,* and for 5Ir/Si-Al$_2$O$_3$ *CCR* samples, respectively (Fig. S15).

3.5. In-situ characterization studies

3.5.1. In-situ FTIR CO adsorption experiments for the analysis of Ir morphology and Ir oxidation state

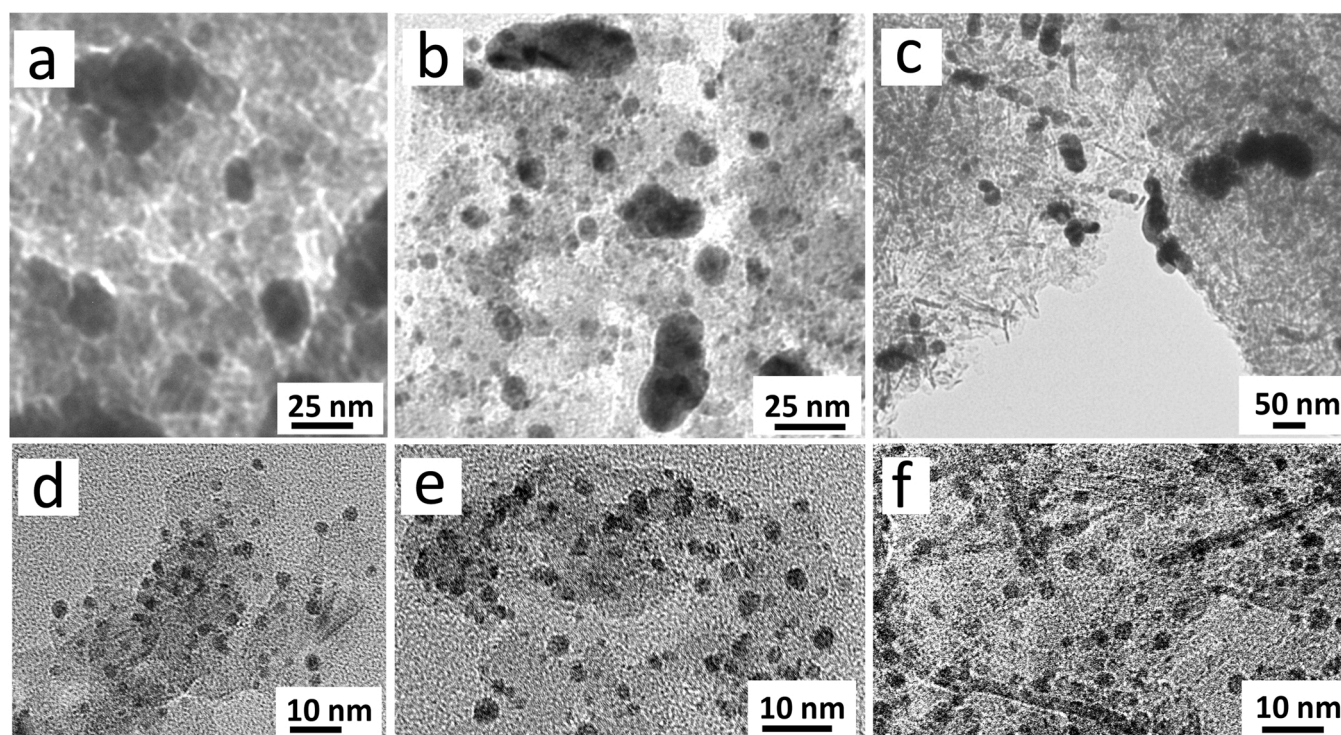In an attempt to investigate the detailed electronic structure of the Ir

Fig. 6. Bright field TEM images of (a) 5Ir/Al$_2$O$_3$ *CCR,* (b) 5Ir/La-Al$_2$O$_3$ *CCR*, (c) 5Ir/Si-Al$_2$O$_3$ *CCR*, (d) 5Ir/Al$_2$O$_3$ *RR*, (e) 5Ir/La-Al$_2$O$_3$ *RR*, and (f) 5Ir/Si-Al$_2$O$_3$ *RR*.
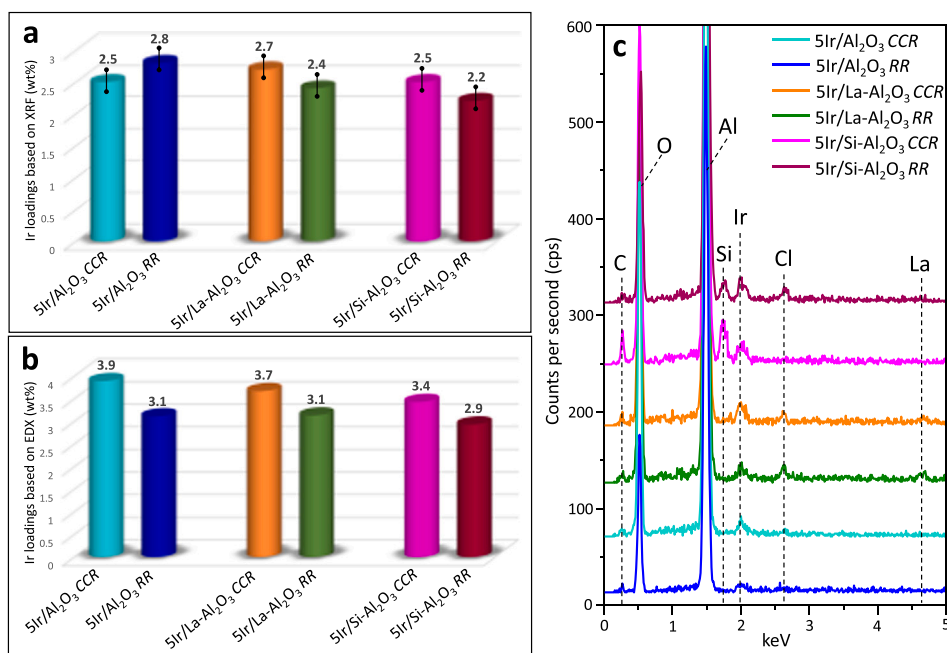
Fig. 7. (a) Ir loadings (wt%) based on XRF, (b) Ir loadings (wt%) based on SEM/EDX, (c) EDX spectra of the investigated catalysts.

active sites and their surface morphology, CO (g) was used as a probe molecule and in-situ FTIR spectroscopic measurements were carried out upon CO adsorption on the synthesized catalysts. Results of these experiments are shown in Fig. 8. Additional in-situ FTIR data corresponding to stepwise increasing CO pressure on each catalyst sample are also provided in Fig. S16.

In-situ FTIR spectra given in Fig. 8 reveal informative results enabling detailed analysis of the electronic structure of the Ir active sites on the synthesized catalyst surfaces. Three different types of CO vibrational features can be identified in Fig. 8a–d which are located at: i) $2091–2082$ cm^{-1}, ii) $2062–2055$ cm^{-1}, and iii) $2079–2070$ cm^{-1} + $2010–2006$ cm^{-1} (Fig. 8e). The first of these vibrational features within $2091–2082$ cm^{-1} can be assigned to atop/ontop/linear adsorption of CO on small and highly dispersed oxidic iridium clusters (Ir$_n^{x+}$
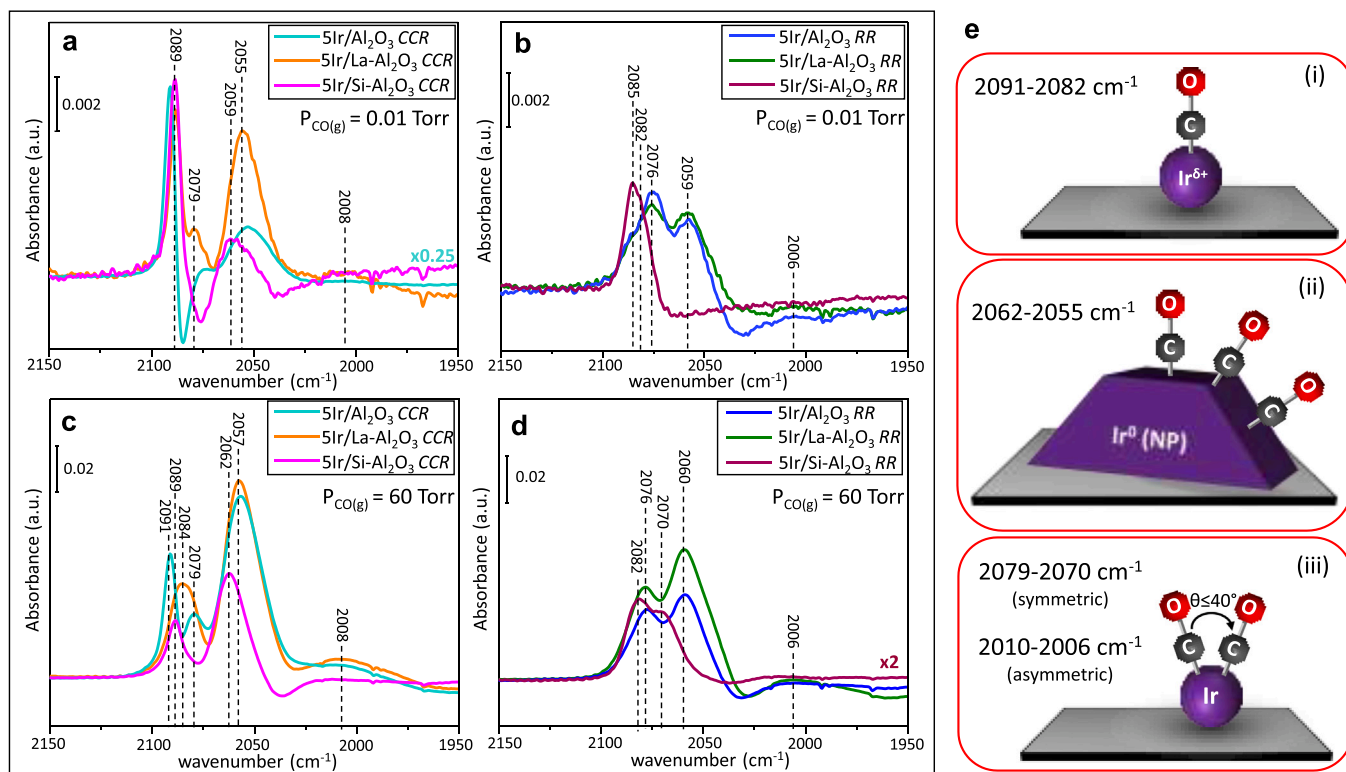

Fig. 8. In-situ FTIR spectra for the synthesized *CCR* and *RR* catalysts upon CO adsorption at (a and b) 0.01 Torr, (c and d) 60 Torr. (e) Schematic representation of CO vibrational features observed for the *CCR* and *RR* catalysts.

as well as atomically dispersed Ir^{x+} [40–42]. Extremely small full width at half maximum (FWHM) values (6–20 cm^{-1}) of this vibrational feature strongly indicates the structural homogeneity of these Ir_n^{x+} sites which is consistent with the small number of Ir atoms in these clusters due to cluster diameters of less than 1 nm [43]. The second vibrational feature observed within 2062–2055 cm^{-1} can be attributed to atop/ontop/linear adsorption of CO on metallic Ir sites (Ir^0) of relatively larger iridium nanoparticles (NP) [40,44–48]. The last vibrational feature consists of a pair of stretchings located within 2079–2070 cm^{-1} (symmetric stretch, *s*) and 2010–2006 cm^{-1} (antisymmetric stretch, *as*) which is associated to gem carbonyls ($Ir(CO)_2$) [41,48–51]. Furthermore, using the expression: $I_{as}/I_s = tan^2\,(\theta/2)$ [41], one can estimate the OC-Ir-CO bond angle *(θ)* in these gem carbonyls to be $\leq 40°$.

Fig. 8a suggests that upon lower CO exposures (i.e., 0.01 Torr) on 5Ir/Al$_2$O$_3$ *CCR*, 5Ir/La-Al$_2$O$_3$ *CCR,* and 5Ir/Si-Al$_2$O$_3$ *CCR* catalysts, coordinatively unsaturated Ir_n^{x+} sites are predominantly populated with carbonyls, where CO adsorption on Ir^0(NP) sites occurs to a lesser extent. Increasing the CO pressure to 60 Torr on these samples (Fig. 8c) indicate saturation of the Ir_n^{x+} sites with carbonyls, whereas Ir^0 (NP) sites continue to adsorb CO species in both samples and the gem carbonyls also become more visible for 5Ir/Al$_2$O$_3$ and 5Ir/La-Al$_2$O$_3$ *CCR* catalyst. These observations are in particularly good agreement with the current XRD data for the *CCR* catalysts revealing the presence of large metallic Ir NP (Fig. 4a) and the interpretation of the current TEM data (Fig. 6a–c) corresponding to a multimodal Ir surface distribution comprised of both large (> 10 nm) and small (2–10 nm) Ir-NP, as well as even smaller Ir clusters of < 1 nm.

Fig. 8b and d present the corresponding in-situ FTIR spectra for the 5Ir/Al$_2$O$_3$ *RR*, 5Ir/La-Al$_2$O$_3$ *RR* and 5Ir/Si-Al$_2$O$_3$ *RR* catalysts. Interestingly, low pressure CO adsorption on the 5Ir/Si-Al$_2$O$_3$ *RR* catalyst shows an unusual behavior which is not observed in any of the other currently investigated catalysts. It is apparent that 5Ir/Si-Al$_2$O$_3$ *RR* catalyst reveals almost exclusively Ir_n^{x+} sites belonging to small Ir clusters. Furthermore, overall FTIR signal intensities of the 5Ir/Si-Al$_2$O$_3$ *RR* sample for high CO coverages (i.e., 60 Torr) is much smaller than all other investigated samples. This is rather surprising since, 5Ir/Si-Al$_2$O$_3$ *RR* sample has a higher SSA than 5Ir/Al$_2$O$_3$ and 5Ir/La-Al$_2$O$_3$ catalysts (Fig. 5). This observation can be explained using the fact that Ir particles may be covered with SiO$_x$-AlO$_x$ domains via SMSI phenomena rendering them less accessible for CO adsorption [42,52]. Likewise, small Ir_n^{x+} clusters also presumably interact strongly with the SiO$_x$-AlO$_x$ surface and become less exposed to CO(g) due to the partial immersion/diffusion of Ir sites into the SiO$_x$-AlO$_x$ matrix. This argument will be further verified with the current in-situ EXAFS measurements demonstrating a greater extent of Ir-O coordination for the 5Ir/Si-Al$_2$O$_3$ *RR* sample. Upon increasing the CO pressure to 60 Torr, 5Ir/Si-Al$_2$O$_3$ *RR* catalyst mostly reveals vibrational features due to Ir_n^{x+} sites and $Ir(CO)_2$ (gem carbonyls), lacking any noticeable FTIR signals associated with Ir^0 NPs. Thus, the unusual ΔP values observed in the catalytic ADN decomposition tests for the 5Ir/Si-Al$_2$O$_3$ *RR* catalyst can be linked to the unique structural/electronic properties of the Ir/SiO$_x$-AlO$_x$ interfacial chemistry which is dominated by small Ir_n^{x+} clusters strongly interacting with the SiO$_x$-AlO$_x$ domains. Si-promotion of alumina may also have an influence on the interaction between the ADN reactant fuel mixture and the catalyst surface. It is known that SiO$_x$ promotion increases the surface acidity of alumina [28]. The higher surface acidity of the Si promoted samples are also verified with pyridine adsorption experiments shown in Fig. S17. Stabilizers used in the ADN fuel mixture such as ammonia result to a basic pH. Thus, increased surface acidity upon Si promotion may lead to poisoning of the 5Ir/Si-Al$_2$O$_3$ *RR* catalyst surface with strongly bound basic (ammonia/amine) groups as well as ADN species which may lead to an increased T_{Onset} (Fig. 3a). ADN adsorption experiments shown in Fig. S18 also illustrate the greater amount of ADN uptake by 5Ir/Si-Al$_2$O$_3$ catalysts. However, upon sufficient thermal activation and liberation of catalytic active sites, basic ammonia/amine groups may desorb from the 5Ir/Si-Al$_2$O$_3$ *RR* catalyst surface and the

remaining large amount of ADN strongly adsorbed on the small Ir_n^{x+} clusters may lead to a high concentration of products resulting in a large ΔP generation. The lack of such a ΔP boost in the case of 5Ir/Si-Al$_2$O$_3$ *CCR* catalyst can be explained by simultaneous desorption of ADN and basic species from the small and large metallic Ir NP (due to the presumably weaker adsorption of ADN on these latter Ir species) which are the predominant Ir species on this catalyst.

In-situ FTIR data for the 5Ir/Al$_2$O$_3$ *RR* and 5Ir/La-Al$_2$O$_3$ *RR* samples given in Fig. 8b and d indicate that on these catalysts, relative surface concentration of Ir_n^{x+} sites are less than the remaining catalyst samples where atop/linear/ontop CO adsorption on Ir^0 NP sites and $Ir(CO)_2$ are the most prominent species. Accordingly, lower T_{Onset} values observed for these catalysts can be attributed to the dominance of Ir^0 NP sites, where ADN decomposition presumably occurs with a lower activation energy. These in-situ FTIR results were typically consistent with the Ir oxidation states obtained from the Ir4f XPS data given in Fig. S19.

3.5.2. Determination of the relative number of exposed surface Ir species via CO chemisorption and CO-TPD experiments

In order to compare the relative number of Ir species on the synthesized catalyst surfaces that are exposed/accessible to CO adsorption, TPD experiments were executed for identical masses of catalysts (ca. 20 mg) and the results are presented in Fig. 9 and Fig. S20. Furthermore, Ir surface dispersion percentages of the catalysts were determined from the CO chemisorption experiments (Fig. 9 and Table S3). In accordance with the in-situ FTIR data given in Fig. 8, despite the fact that Si-promoted catalysts have significantly higher SSA (Fig. 5), they adsorb significantly lower amounts of CO and the Ir dispersion is lower as compared to that of 5Ir/Al$_2$O$_3$ and 5Ir/La-Al$_2$O$_3$ samples. This can be explained by the relatively higher surface acidity of the Si-promoted alumina support material restricting CO uptake by the support, as well as the SMSI phenomena rendering Ir sites less accessible to CO due to blockage of Ir sites with SiO$_x$-AlO$_x$. The highest Ir dispersion and CO uptake is observed for the 5Ir/La-Al$_2$O$_3$ *RR* sample which can be attributed to i) a less acidic La-promoted alumina support material enabling direct CO uptake by the support as well as spill-over of CO from the La-promoted alumina support to Ir active sites, ii) predominantly metallic Ir NP (Fig. 8d) facilitating CO adsorption.

3.5.3. In-situ XANES/EXAFS experiments for analyzing Ir nearest neighbors and coordination

Initial XANES/EXAFS experiments were carried out on a metallic Ir foil for energy calibration and optimization of the EXAFS fitting parameters (Fig. S21). Details of the EXAFS best fitting parameters for all investigated catalysts also presented in Table S4 and the corresponding XANES/EXAFS data are shown in Fig. 10a–l. Fig. 10a–d depict the EXAFS data obtained after the final reduction step of the in-situ catalyst synthesis protocol as described in the experimental section, while the EXAFS results presented in Fig. 10e–h are associated with the consecutive exposure of these samples to O$_2$ flow at RT. Corresponding XANES spectra for these EXAFS results are given in Fig. 10i–l.

Current EXAFS results (Table S4 and Fig. 10a) suggest that Ir/La-Al$_2$O$_3$ *RR* catalyst is mostly comprised of metallic Ir species due to Ir-Ir coordination. This is in particularly good agreement with the corresponding in-situ FTIR data illustrated in Fig. 8b and d, revealing the lack of a large extent of Ir_n^{x+} species. It is seen that exposure of this catalyst to O$_2$ leads to the partial oxidation of the Ir species evident by both EXAFS data (Table S4 and Fig. 10e) suggesting the generation of Ir-O coordination signals and the XANES data (Fig. 10i) indicating an increase in the Ir L$_{III}$-edge white line intensity [53,54].

In stark contrast, 5Ir/Si-Al$_2$O$_3$ *RR* catalyst (Table S4 and Fig. 10b) possesses larger extent of Ir-O coordination which is in excellent accordance with the presence of Ir_n^{x+} species suggested by the in-situ FTIR data depicted in Fig. 8b and d. As this particular catalyst did not undergo any calcination treatment, the oxide ions of the support material are the only source for oxygen. This also indicates the presence of the
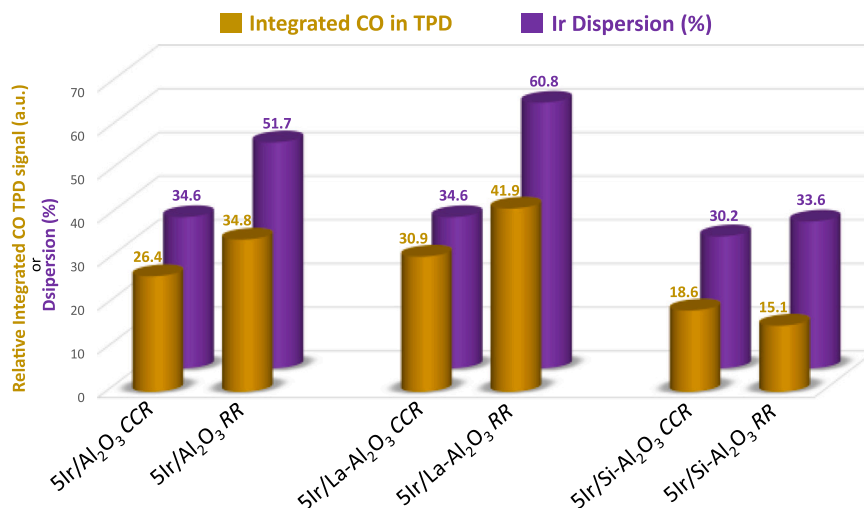
Fig. 9. Integrated relative CO-TPD desorption signals and Ir surface dispersion values obtained from CO chemisorption experiments for the investigated catalysts with identical masses.
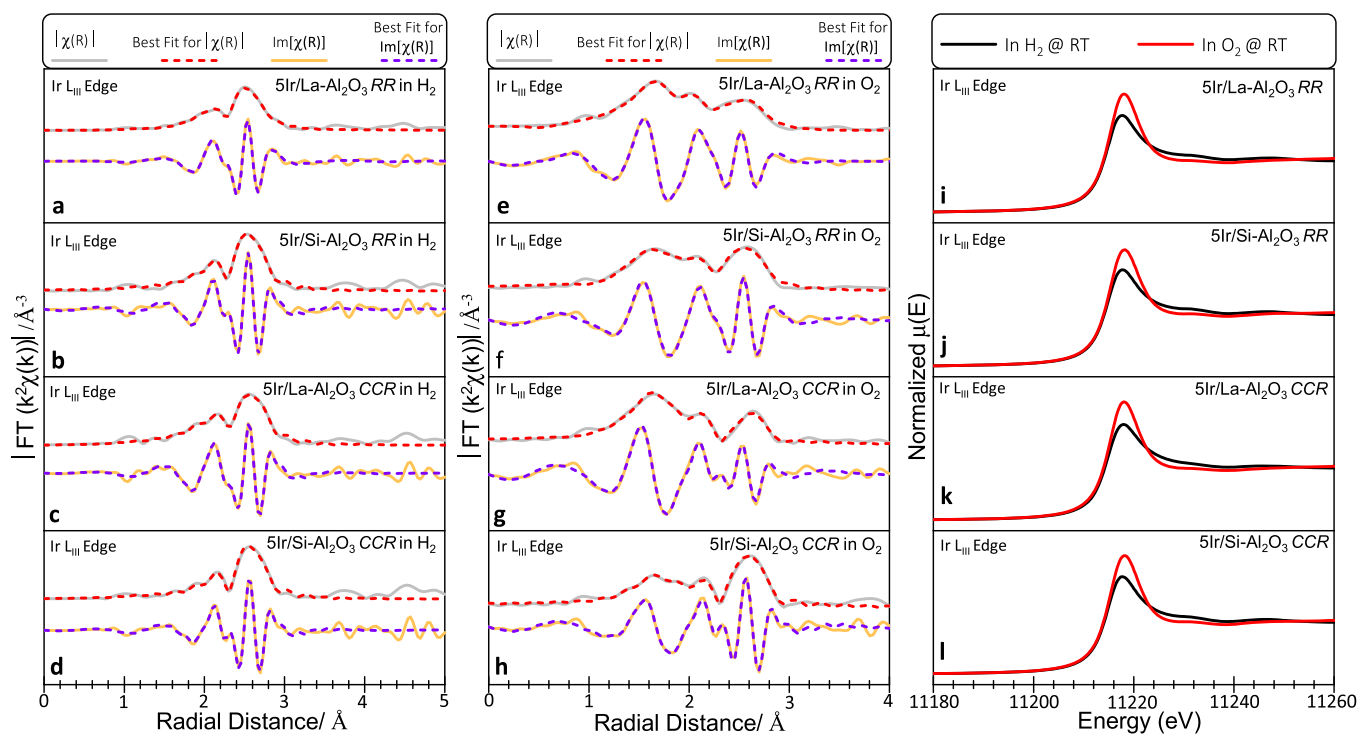

Fig. 10. In-situ EXAFS data obtained (a–d) after the final reduction step of the catalyst preparation protocol and (e-h) consecutive exposure of these catalysts to O_2 flow (see text for details). (i–l) Corresponding Ir L_{III} edge XANES data for the experiments shown in parts (a–h).

strong interaction between Ir sites and the SiO_x-AlO_x support surface. Oxidation of this sample in O_2 (Table S4 and Fig. 10f) also leads to the most oxidic Ir species among all other investigated catalysts, which is in line with the presence of a large concentration of highly reactive Ir_n^{x+} clusters on the 5Ir/Si-Al$_2$O$_3$ *RR* catalyst that can readily undergo oxidation (Fig. 10j).

EXAFS data for 5Ir/La-Al$_2$O$_3$ *CCR* catalyst (Table S4 and Fig. 10c) reveals prominently metallic Ir species with Ir-Ir coordination and a limited extent of oxidic Ir species as expected from the current XRD (Fig. 4a) and in-situ FTIR spectroscopy (Fig. 8a and c) data. Oxidation of this sample augments the extent of Ir-O coordination (Table S4 and Fig. 10g) and increases the Ir oxidation state (Fig. 10k).

Finally, 5Ir/Si-Al$_2$O$_3$ *CCR* catalyst possesses the second most oxidic Ir

species (Table S4 and Fig. 10d). These iridium species can be further oxidized upon O_2 exposure (Fig. 10h and l).

4. Conclusion

In this study, we focused on the structural origins of the catalytic promotional effects on the anaerobic decomposition of ADN on 5Ir/Al$_2$O$_3$, 5Ir/La-Al$_2$O$_3$ and 5Ir/Si-Al$_2$O$_3$ catalysts where La and Si were chosen as two different types of promoters. We also investigated the influence of the variations in the catalyst preparation protocols (*CCR* vs. *RR*) on the catalyst structure and catalytic performance parameters such as the onset temperature (T_{Onset}) and the pressure generation during the reaction (ΔP_{max} and ΔP_{eq}). Our findings can be summarized as follows;.

5Ir/Al$_2$O$_3$ and 5Ir/La-Al$_2$O$_3$: i) lead to lower T$_{Onset}$ but also smaller ΔP$_{max}$ and ΔP$_{eq}$ values where catalyst preparation protocols (*CCR* vs. *RR*) had a less significant effect on T$_{Onset}$, ii) form δ-Al$_2$O$_3$ and γ-Al$_2$O$_3$ phases with a relatively lower specific surface area (SSA), iii) result in the formation of predominantly metallic Ir nanoparticles along with oxidic Ir^{x+} species as minority species and these metallic Ir species are dispersed on these materials in a multimodal manner lowering the activation energy (*E$_a$*) of the ADN decomposition reaction. Effect of La promotion on T$_{Onset}$, ΔP$_{max}$ and ΔP$_{eq}$ values is limited. On the other hand, La promotion improves the structural stability of the alumina support by assisting the preservation of the SSA of the support at high temperatures.

5Ir/Si-Al$_2$O$_3$: i) yields higher T$_{Onset}$ values, but (particularly *RR* preparation protocol) leads to a significant boost in the ΔP$_{max}$ and ΔP$_{eq}$ values, ii) results in the exclusive formation of γ-Al$_2$O$_3$ phase with extremely high SSA, iii) leads to the formation of oxidic Ir$_n^{x+}$ clusters which strongly interact with the SiO$_x$-AlO$_x$ domains leading to partial blocking/covering of the Ir sites with the SiO$_x$-AlO$_x$ domains via strong metal support interaction (SMSI).

Along these lines, it can be envisaged that next generation catalytic architectures can be designed for ADN decomposition using the fundamental molecular level insight provided in the current study where novel synthetic protocols can be developed to enable the preparation of bi-functional Ir active sites, including metallic Ir NPs lowering the T$_{Onset}$ and E$_a$ as well as oxidic Ir clusters (Ir$_n^{x+}$) capable of boosting ΔP to generate enhanced thrust.

Funding sources

Author contributions

E. Ozensoy conceived the study, designed the experiments/instrumental setup, and constructed the research plan. **A. Koc**, and **H. Esiyok** synthesized ADN fuel formulations and performed fuel quality control experiments. **B.S. Caglayan** and **A.E. Aksoylu** carried out Ir dispersion via CO chemisorption, XRF measurements, and relevant data analysis. **Y. Koçak** conducted the XPS measurements and associated data analysis. **M. Kurt** and **Abel. T. Sika-Nartey** performed in-situ FTIR and TPD experiments. **M. Kurt**, **Z. Kap**, and **S. Senol** synthesized the catalysts and carried out catalytic micro-reactor performance tests, XRD, BET, ATR-IR, TEM, and EDX experiments and the corresponding data analyses. **Kerem E. Ercan** performed DSC/TGA/FTIR, XANES/EXAFS measurements and associated data analyses. All authors discussed the results and contributed to the manuscript.

Declaration of Competing Interest

The authors declare that they have no known competing financial interests or personal relationships that could have appeared to influence the work reported in this paper.

Acknowledgments

Appendix A. Supporting information

Supplementary data associated with this article can be found in the online version at doi:10.1016/j.apcata.2022.118500.

References

[1] E.W. Schmidt, E.J. Wucherer, in: Proc. 2nd Int. Conference on Green Propellants for Space Propulsion ESA SP-557, 2004.
[2] E.W. Schmidt, Hydrazine and Its Derivatives: Preparation, Properties, Application, John Wiley & Sons, New York, 2001.
[3] H.N. Nguyen MC USAF, J.A. Chenoweth MD MAS, V.S. Bebarta MC USAF, T. E. Albertson USA (Ret.), C.D. Nowadly MC USAF, Mil. Med. 186 (2021) e319–e326, https://doi.org/10.1093/milmed/usaa429.
[4] European Chemicals Agency (ECHA), Hydrazine - substance information ⟨https://echa.europa.eu/substance-information/-/substanceinfo/100.005.560⟩.
[5] R.L. Sackheim, R.K. Masse, J. Propuls. Power 30 (2014) 265–276, https://doi.org/10.2514/1.B35086.
[6] Q. Zhang, J.M. Shreeve, Chem. Rev. 114 (2014) 10527–10574, https://doi.org/10.1021/cr500364t.
[7] D. Freudenmann, H.K. Ciezki, Propellants, Explos. Pyrotech. 44 (9) (2019) 1084–1089, https://doi.org/10.1002/prep.201900127.
[8] R. Amrousse, T. Katsumi, N. Itouyama, N. Azuma, H. Kagawa, K. Hatai, H. Ikeda, K. Hori, Combust. Flame 162 (2015) 2686–2692, https://doi.org/10.1016/j.combustflame.2015.03.026.
[9] Courthéoux, S. Rossignol, C. Kappenstein, N. Pillet, in: 39th AIAA/ASME/SAE/ASEE Jt. Propuls. Conf. Exhib., 2003, ⟨https://doi.org/10.2514/6.2003–4645⟩.
[10] H.F.R. Schoyer, W.H.M. Welland-Veltmans, J. Louwers, P. Korting, A. Van der Heijden, H.L.J. Keizers, R.P. Van den Berg, J. Propuls. Power 18 (2002) 138–145, https://doi.org/10.2514/2.5909.
[11] C. Oommen, S.R. Jain, J. Hazard. Mater. 67 (1999) 253–281, https://doi.org/10.1016/S0304-3894(99)00039-4.
[12] M. Negri, M. Wilhelm, C. Hendrich, N. Wingborg, L. Gediminas, L. Adelöw, C. Maleix, P. Chabernaud, R. Brahmi, R. Beauchet, Acta Astronaut 143 (2018) 105–117, https://doi.org/10.1016/j.actaastro.2017.11.016.
[13] N. Wingborg, C. Eldsäter, H. Skifs, Proc. 2nd Int. Conference on Green Propellants for Space Propulsion ESA SP-557, 2004.
[14] P. Friedhoff K. Anflo P. Thormahlen M. Persson in: 54th AIAA/ASME/SAE/ASEE Jt Propuls. Conf. Exhib. 2018.https://doi.org/10.2514/6.2018-4754.
[15] A. Larsson, N. Wingborg, Green propellants based on ammonium dinitramide (ADN), Dr Jason Hall (Ed.), Advances in spacecraft technologies, 2011. ISBN: 978-953-307-551-8.
[16] J. Chen, G. Li, T. Zhang, M. Wang, Y. Yu, Acta Astronaut 129 (2016) 367–373, https://doi.org/10.1016/j.actaastro.2016.09.027.
[17] C. Maleix, P. Chabernaud, R. Brahmi, R. Beauchet, Y. Batonneau, C. Kappenstein, M. Schwentenwein, R.-J. Koopmans, S. Schuh, C. Scharlemann, Acta Astronaut 158 (2019) 407–415, https://doi.org/10.1016/j.actaastro.2017.11.016.
[18] N.C. Newton, P.R. Rice, D.D. Nuxtable, Shell 405 Catalyst Improvement Substrate Evaluation, Technical Report Air Force Rocket Propulsion Laboratory (AFRPL –TR – pp. 71–81), 1971.
[19] W.E. Armstrong, L.B. Ryland, H.H. Voge, US Patent 4,124,538, 1978.
[20] R.T.K. Baker, R.D. Sherwood, J. Catal. 61 (1980) 378–389, https://doi.org/10.1016/0021-9517(80)90385-1.
[21] R.J. Seymour, J. O'Farrelly, Platinum-group Metals. Kirk-Othmer Encycl. Chem. Technol., John Wiley & Sons, Inc, Hoboken, NJ, USA, 2012, pp. 1–37, https://doi.org/10.1002/0471238961.1612012019052513.a01.
[22] J. Lin, L. Li, X. Pan, X. Wang, Y. Cong, T. Zhang, S. Zhu, AIChE J. 62 (2016) 3973–3981, https://doi.org/10.1002/aic.15324.
[23] T. Katsumi, K. Hori, Energ. Mater. Front. 2 (2021) 228–237, https://doi.org/10.1016/j.enmf.2021.09.002.
[24] S. Rossignol, C. Kappenstein, Int. J. Inorg. Mater. 3 (2001) 51–58, https://doi.org/10.1016/S1466-6049(00)00088-X.
[25] J. Yang, Q. Wang, T. Wang, Y. Liang, RSC Adv. 6 (2016) 26271–26279, https://doi.org/10.1039/C5RA28053B.
[26] B.R. Goldsmith, B. Peters, J.K. Johnson, B.C. Gates, S.L. Scott, ACS Catal. 7 (2017) 7543–7557, https://doi.org/10.1021/acscatal.7b01767.
[27] A.A. Vedyagin, R.M. Kenzhin, M.Y. Tashlanov, E.A. Alikin, V.O. Stoyanovskii, P. E. Plyusnin, Y.V. Shubin, I.V. Mishakov, M.Y. Smirnov, A.V. Kalinkin, V. I. Bukhtiyarov, Top. Catal. 63 (2020) 152–165, https://doi.org/10.1007/s11244-019-01213-x.
[28] F. Rascón, R. Wischert, C. Copéret, Chem. Sci. 2 (2011) 1449–1456, https://doi.org/10.1039/C1SC00073J.
[29] M. Li, D. Weng, X. Wu, J. Wan, B. Wang, Catal. Today 201 (2013) 19–24, https://doi.org/10.1016/j.cattod.2012.03.047.
[30] E. Kayhan, S.M. Andonova, G.S. Şentürk, C.C. Chusuei, E. Ozensoy, J. Phys. Chem. C 114 (2010) 357–369, https://doi.org/10.1021/jp907982q.
[31] A.J. Saadun, G. Zichittella, V. Paunović, B.A. Markaide-Aiastui, S. Mitchell, J. Pérez-Ramírez, ACS Catal. 10 (2020) 528–542, https://doi.org/10.1021/acscatal.9b04467.
[32] S. Hinokuma, T. Iwasa, Y. Kon, T. Taketsugu, K. Sato, Catal. Commun. 149 (2021), 106208, https://doi.org/10.1016/j.catcom.2020.106208.
[33] ROCK | French national synchrotron facility. ⟨https://www.synchrotron-soleil.fr/en/beamlines/rock⟩.

[34] B. Ravel, M. Newville, J. Synchrotron Radiat. 12 (2005) 537–541, https://doi.org/10.1107/S0909049505012719.

[35] SAMBA | French national synchrotron facility. ⟨https://www.synchrotron-soleil.fr/en/beamlines/samba⟩.

[36] L. Jing, J. Huo, H. Wang, X. You, M. Zhu, Y. Yang, Z. Yao, J. Propuls. Power 33 (2016) 343–349, https://doi.org/10.2514/1.B36342.

[37] S. Löbbecke, H.H. Krause, A. Pfeil, Propellants, Explos. Pyrotech. 22 (1997) 184–188, https://doi.org/10.1002/prep.19970220317.

[38] ⟨https://webbook.nist.gov⟩.

[39] H. Arai, M. Machida, Appl. Catal. A Gen. 138 (1996) 161–176, https://doi.org/10.1016/0926-860X(95)00294-4.

[40] F.J.C.M. Toolenaar, A.G.T.M. Bastein, V. Ponec, J. Catal. 82 (1983) 35–44, https://doi.org/10.1016/0021-9517(83)90115-X.

[41] Y. Lu, J. Wang, L. Yu, L. Kovarik, X. Zhang, A.S. Hoffman, A. Gallo, S.R. Bare, D. Sokaras, T. Kroll, V. Dagle, H. Xin, A.M. Karim, Nat. Catal. 2 (2019) 149–156, https://doi.org/10.1038/s41929-018-0192-4.

[42] L. Chen, I.S. Ali, G.E. Sterbinsky, X. Zhou, E. Wasim, S.L. Tait, Catal. Sci. Technol. 11 (2021) 2081–2093, https://doi.org/10.1039/D0CY01132K.

[43] A.S. Hoffman, C.-Y. Fang, B.C. Gates, J. Phys. Chem. Lett. 7 (2016) 3854–3860, https://doi.org/10.1021/acs.jpclett.6b01825.

[44] G.B. McVicker, R.T.K. Baker, R.L. Garten, E.L. Kugler, J. Catal. 65 (1980) 207–220, https://doi.org/10.1016/0021-9517(80)90295-X.

[45] L. Lynds, Spectrochim. Acta 20 (1964) 1369–1372, https://doi.org/10.1016/0371-1951(64)80117-X.

[46] P. Gélin, A. Auroux, Y. Ben Taarit, P.C. Gravelle, Appl. Catal. 46 (1989) 227–240, https://doi.org/10.1016/S0166-9834(00)81119-7.

[47] F. Solymosi, É. Novák, A. Molnár, J. Phys. Chem. 94 (1990) 7250–7255, https://doi.org/10.1021/j100381a054.

[48] T. Beutel, S. Kawi, S.K. Purnell, H. Knoezinger, B.C. Gates, J. Phys. Chem. 97 (1993) 7284–7289, https://doi.org/10.1021/j100130a027.

[49] K. Tanaka, K.L. Watters, R.F. Howe, J. Catal. 75 (1982) 23–38, https://doi.org/10.1016/0021-9517(82)90118-X.

[50] P. Gelin, G. Coudurier, Y.B. Taarit, C. Naccache, J. Catal. 70 (1981) 32–40, https://doi.org/10.1016/0021-9517(81)90314-6.

[51] M. Mihaylov, E. Ivanova, F. Thibault-Starzyk, M. Daturi, L. Dimitrov, K. Hadjiivanov, J. Phys. Chem. B 110 (2006) 10383–10389, https://doi.org/10.1021/jp057128t.

[52] P. Reyes, M.C. Aguirre, G. Pecchi, J.L.G. Fierro, J. Mol. Catal. A Chem. 164 (2000) 245–251, https://doi.org/10.1016/S1381-1169(00)00329-0.

[53] F.J. Gracia, L. Bollmann, E.E. Wolf, J.T. Miller, A.J. Kropf, J. Catal. 220 (2003) 382–391, https://doi.org/10.1016/S0021-9517(03)00296-3.

[54] K. Jiang, M. Luo, M. Peng, Y. Yu, Y.-R. Lu, T.-S. Chan, P. Liu, F.M.F. de Groot, Y. Tan, Nat. Commun. 11 (2020) 2701, https://doi.org/10.1038/s41467-020-16558-1.